We are IntechOpen, the world's leading publisher of Open Access books Built by scientists, for scientists

4,800
Open access books available

122,000
International authors and editors

135M
Downloads

Our authors are among the

154
Countries delivered to

TOP 1%
most cited scientists

12.2%
Contributors from top 500 universities

WEB OF SCIENCE™

Selection of our books indexed in the Book Citation Index in Web of Science™ Core Collection (BKCI)

Interested in publishing with us?
Contact book.department@intechopen.com

Numbers displayed above are based on latest data collected.
For more information visit www.intechopen.com

12

The Numerical Simulation of Hydrodynamics of Fishing Net Cage

Yunpeng Zhao[1,*], Tiaojian Xu[1], Chunwei Bi[1], Guohai Dong[1] and Shengcong Liu[2]
[1]*Dalian University of Technology*
[2]*Dalian Tianzheng Industry Co., Ltd*
China

1. Introduction

The aquaculture industry is playing an increasingly important role in the fish production industry as the demand for seafood increases. At present, the net cage is widely used in aquaculture industry all over the world. Because of environmental impact concerns and limited near-shore locations, more and more net cages for aquaculture will be located offshore and exposed to more waves and currents. Thus, knowledge of their hydrodynamic behavior of net cage under the action of waves and current is of great importance to the design of gravity cages in the open sea.

Techniques used to investigate the facilities have typically included the use of scaled physical and numerical models, and, where possible, field measurements. Comparing model tests and field measurement, the numerical simulation method is low in cost, saving time and being easy to manage. In this chapter, the latest progress of this technology by our research group will be introduced in detail. The contents of the progresses include the following parts: *The numerical simulation of net cage in irregular waves; The numerical simulation of multi-net cage in waves; The numerical simulation of flow through and around fishing net cage.*

2. Numerical methods

The fishing net cage is mainly composed of two parts: floating collar and fishing net. The floating collar is model as a rigid body and the fishing net is simulated as flexible body. The numerical model of net cage system is described in detail as follow.

2.1 Fishing net

By applying the lumped-mass model, the net is assumed to be a connected structure with springs and limited mass points, which are set at each knot and the centre of the mesh bar, as shown in Fig. 1. According to the Newton's second law, the motion equation of lumped mass in waves can be written as follows:

*Corresponding author

$$M\ddot{\vec{R}} = M\frac{\partial^2 \vec{R}}{\partial t^2} = \vec{F}_D + \vec{F}_I + \vec{T} + \vec{B} + \vec{W} \tag{1}$$

where $\vec{F}_D$ and $\vec{F}_I$ are the drag and inertia forces, respectively, $\ddot{\vec{R}}$ is the acceleration of mass point, $\vec{T}$ is the tension force in twine, $\vec{B}$ is the buoyancy force, and $\vec{W}$ is the gravity force. According to the research of **Zhao et al. (2008)**, the inertial force $\vec{F}_I$ on fishing net in waves is much smaller than drag force, so here it is omitted.

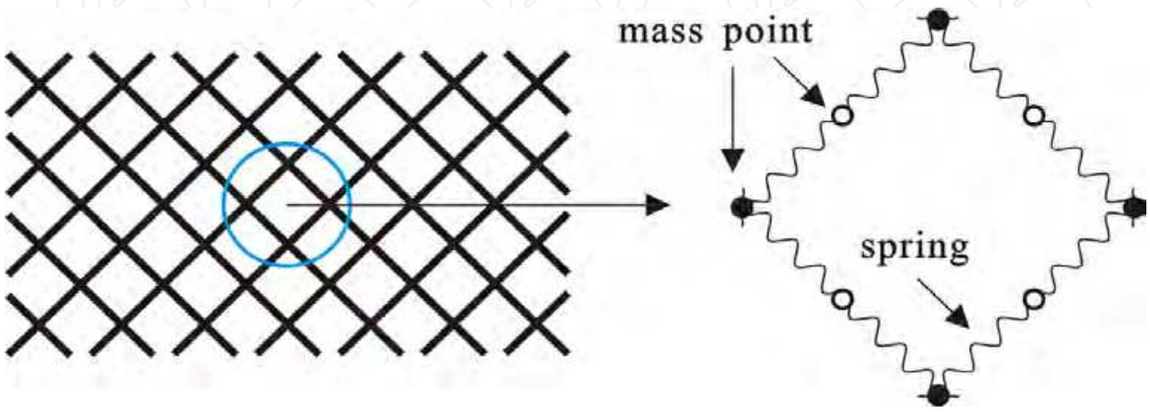

Fig. 1. Schematic of mass-spring model for net pen

The relationship between the elastic elongation of twine and tension based on **Wilson (1967)** is given by:

$$T = d^2 C_1 \varepsilon^{C_2}, \quad \varepsilon = \frac{l - l_0}{l_0} \tag{2}$$

where T is the tension force in twine, l_0 is the undeformed length of twine, l is the deformed length, d is the diameter of twine, C_1 and C_2 are the elastic constants of material which can be obtained by matching, referring to **Gerhard (1983)**. For polyethylene (PE), C_1=345.37×10^6, and C_2=1.0121; for polyamide (PA), C_1=784.9×10^6, and C_2=1.6988. The units of T and d are N and m, respectively.

To consider the direction of fluid forces acting on net mesh bar, a local coordinate system O-$\tau\eta\xi$ is defined, as described by Fig. 2. The origin of the local coordinate system is set at the centre of a mesh bar and the η axis lies on the plane including τ and V.

Besides the gravity and buoyancy, the τ component of the drag force on lumped-mass point can be obtained by Morison Equation, as follows.

$$F_{D\tau} = \frac{1}{2}\rho C_{D\tau} D l \left|\vec{V}_\tau - \dot{\vec{R}}_\tau\right| (\vec{V}_\tau - \dot{\vec{R}}_\tau) \tag{3}$$

where $C_{D\tau}$ represents the drag coefficient of the τ component, D is the diameter of twine, and l is its length. The same expression can be applied to the other drag forces ($F_{D\eta}$, $F_{D\xi}$) of η, ξ components. The drag coefficients related to Reynolds number are described in following section.

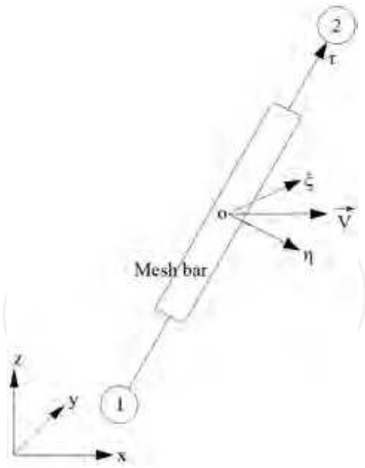

Fig. 2. Schematic diagram of the local coordinates for mesh yarns

For each mesh bar, the numerical procedure calculates the drag coefficient C_n and C_τ using a method described by **Choo and Casarella (1971)** that updates the drag coefficients based on the Reynolds number (Re_n) as follows:

$$C_n = \begin{cases} \dfrac{8\pi}{\mathrm{Re}_n s}\left(1-0.87s^{-2}\right) & \left(0<\mathrm{Re}_n\le 1\right) \\ 1.45+8.55\mathrm{Re}_n^{-0.90} & \left(1<\mathrm{Re}_n\le 30\right) \\ 1.1+4\mathrm{Re}_n^{-0.50} & \left(30<\mathrm{Re}_n\le 10^5\right) \end{cases} \tag{4}$$

$$C_\tau = \pi\mu(0.55\mathrm{Re}_n^{1/2}+0.084\mathrm{Re}_n^{2/3}) \tag{5}$$

where $Re_n=\rho V_{Rn}D/\mu$, s=-0.077215665+ln(8/Re_n), μ is the viscosity of water, C_n and C_τ are the normal and tangential drag coefficients for mesh bar, V_{Rn} is the normal component of the fluid velocity relative to the bar, and ρ is the density of water.

For the knot part, the **Fredheim and Faltinsen (2003)** suggested it could be reasonable to use a drag coefficient in the range of 1.0-2.0 when modeling the knot part as a sphere. Here C_D is set as 1.0 for the knot part.

2.2 Floating collar

2.2.1 Forces on floating collar

Although the float collar mainly consists of two concentric pipe rings and a hand rail. Float collar system is usually at the water surface and double floating pipes are the main components to withstand the wave and current induced loads. For the sake of simplicity, the float collar system is reduced to a double-column pipe structure.

When calculating the forces on float collar, the float collar is divided into many mini-segments. The forces on the whole collar can be obtained by summing the forces on each mini-segment. Fig. 3 is a sketch of a mini-segment of the float collar with a local coordinate

system defined in each mini-segment. As to the coordinate system, n and τ are in the normal and tangential directions of the mini-segment, respectively, and then v is normal to the mini-plane.

Because the tube diameter of float collar is relatively small compared to the wave length. As **Brebbia and Walker (1979)** suggested, the n component of wave-induced forces on a mini-segment can be calculated using the modified Morison equation to include relative motion between the structural element and the surrounding fluid, which is shown as follows:

$$F_n = \frac{1}{2} C_{Dn} \rho A_n \left| \vec{u}_n - \dot{\vec{R}}_n \right| \cdot (\vec{u}_n - \dot{\vec{R}}_n) + \rho V_0 \vec{a}_n + C_{mn} \rho V_0 (\vec{a}_n - \ddot{\vec{R}}_n) \tag{6}$$

where $\vec{u}_n$ and $\dot{\vec{R}}_n$ are the velocity vectors for water particles and mini-segments of the n component, respectively; $\vec{a}_n$ and $\ddot{\vec{R}}_n$ are the acceleration vectors for water particles and mini-segments of the n component, respectively; ρ is the density of water; V_0 is the water displaced volume of a mini-segment; A_n is the effective projected area of a mini-segment in the direction of the n component; and C_{Dn} and C_{mn} are the drag and added mass coefficients of the n component, respectively. The same expression can be applied to other wave-induced forces (F_τ, F_v).

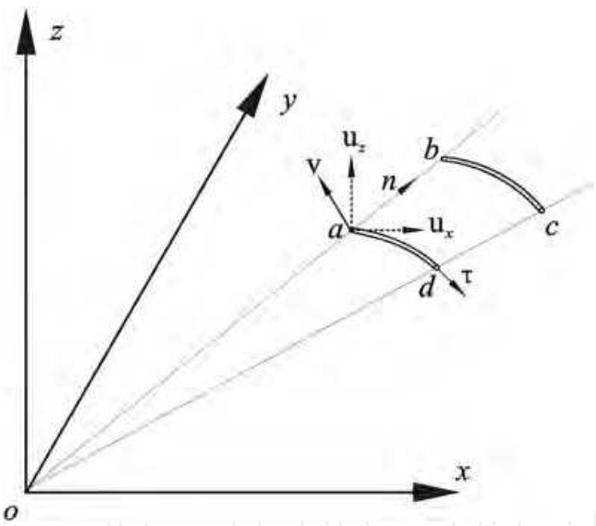

Fig. 3. Sketch of float collar mini-segment

The relationship between the mooring-line forces and elongation is determined experimentally and to be used in the numerical simulation, as follows:

$$T = 10.4 \times (\Delta S / S)^{1.132} \tag{7}$$

where ΔS is the elongation of a mooring line (m), S is the original length of the mooring line (m), and T is the tension in the mooring line (N).

Apart from the above-mentioned external force, the float collar is also subjected to gravity and buoyancy forces. Because it is easy to calculate these forces, the formulation for these forces is not given here.

2.2.2 Motion of floating collar

The three-dimensional motions of the float collar include surge-sway-heave translation and roll-pitch-yaw rotation. To obtain the motions of the float collar, two sets of coordinate systems are defined, which are the fixed-coordinate system *Oxyz*, and the body-coordinate system *G123*, as shown in the Fig. 4. Initially, axes *x*, *y* and *z* are parallel to axes 1, 2 and 3.

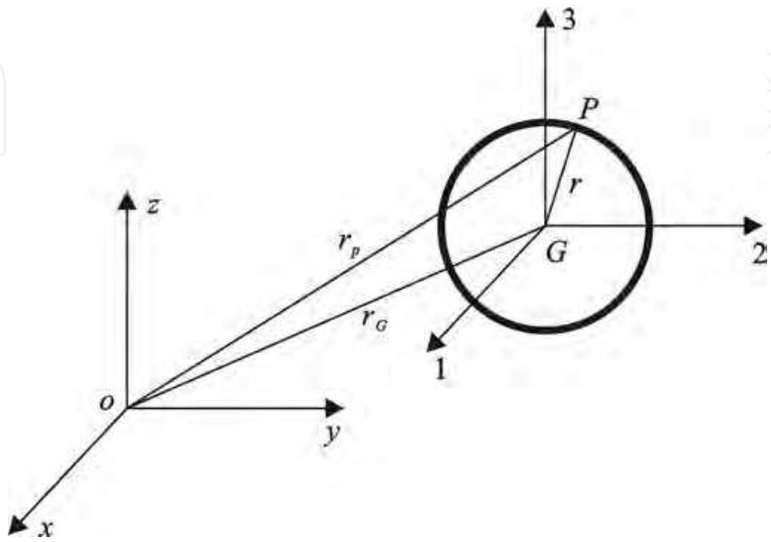

Fig. 4. Schematic of the body-coordinate system of float collar

Six degrees of freedom are required to describe the motion of float collar. According to the Newton's second law, under fixed coordinate system, the three translational equations of motion are given by:

$$\ddot{x}_G = \frac{1}{m_G}\sum_{i=1}^{N} F_{x_i}, \quad \ddot{y}_G = \frac{1}{m_G}\sum_{i=1}^{N} F_{y_i}, \quad \ddot{z}_G = \frac{1}{m_G}\sum_{i=1}^{N} F_{z_i} \tag{8}$$

where F_{xi}, F_{yi} and F_{zi} are the components of the external forces on mini-segment along fixed-coordinate axes *x*, *y* and *z*, m_G is the mass of the float collar, x_G, y_G and z_G are the acceleration of the mass centre of the float collar, and *N* is the number of mini-segments.

Axes 1, 2, 3 are principal axes with origin at the centre of the mass *G*, and thus the Euler equations of motion of a rigid body (**Bhatt and Dukkipati, 2001**) are applied. In the body-coordinate system, the three rotational equations of motion are given by:

$$\begin{gathered} I_1\frac{\partial\omega_1}{\partial t} + (I_3 - I_2)\omega_3\omega_2 = M_1, \quad I_2\frac{\partial\omega_2}{\partial t} + (I_1 - I_3)\omega_1\omega_3 = M_2 \\ I_3\frac{\partial\omega_3}{\partial t} + (I_2 - I_1)\omega_1\omega_2 = M_3 \end{gathered} \tag{9}$$

where subscripts 1, 2, 3 represent the body-coordinate axes 1, 2, 3; I_1, I_2 and I_3 are the components of the moments of inertia *I* along the three principal axes; ω_1, ω_2 and ω_3 are the components of angular velocity vector ω along the three principal axes; M_1, M_2 and M_3 are the components of the moment vector *M* along the three principal axes.

2.3 Flow around fishing net

The numerical simulation of the flow field around a plane net is based on the FLUENT software platform. The porous media model is introduced to model the plane net (see Fig. 5), and the finite volume method (FVM) is used to solve the governing equations of the numerical model. In this way, the numerical simulation of the flow field around the plane net is available.

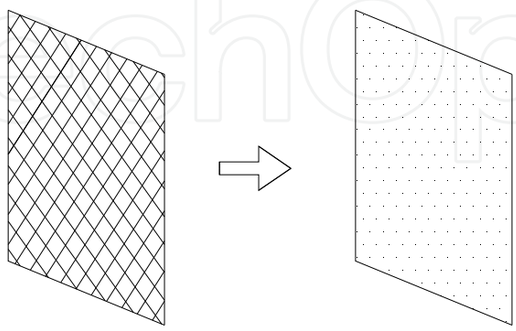

Fig. 5. Sketch of the porous media model.

2.3.1 Porous media resistance coefficients

The porous media model employs empirically determined flow resistance in the region of the porous media **(Fluent, 2006)**. For flow through the porous media, the hydrodynamic forces acting on the porous media can be expressed as follows:

$$F = S_i \lambda A \tag{10}$$

where S_i is the source term for the momentum equation in the i direction, λ is the thickness of the porous media, A is the area of the porous media, and F is the hydrodynamic force in the i direction.

When the region is outside the porous media model, $S_i = 0$. While, inside the porous media, S_i is calculated by the following equation:

$$\begin{aligned} S_i &= -\left(D_{ij}\mu u + C_{ij}\frac{1}{2}\rho |u| u \right); \\ D_{ij} &= \begin{pmatrix} D_n & 0 & 0 \\ 0 & D_t & 0 \\ 0 & 0 & D_t \end{pmatrix}, C_{ij} = \begin{pmatrix} C_n & 0 & 0 \\ 0 & C_t & 0 \\ 0 & 0 & C_t \end{pmatrix}. \end{aligned} \tag{11}$$

where D_{ij} and C_{ij} are prescribed material matrices consisting of the porous media resistance coefficients, D_n is the normal viscous resistance coefficient, D_t is the tangential viscous resistance coefficient, C_n is the normal inertial resistance coefficient, C_t is the tangential inertial resistance coefficient.

Substituting Eq. (11) into Eq. (10) provides formulas for calculating the drag force (F_d) and the lift force (F_l) of the plane net. The drag force is parallel to the flow direction, and the lift force is perpendicular to the flow direction.

$$F_d = \left(D_n \mu u + C_n \frac{1}{2} \rho |u| u \right) \lambda A \tag{12}$$

$$F_l = \left(D_t \mu u + C_t \frac{1}{2} \rho |u| u \right) \lambda A \tag{13}$$

The porous coefficients in Eq. (11) can be calculated by the data for the drag and lift forces. In a general way, the drag and lift forces of the plane net are obtained from the laboratory experiments. In addition, the forces can be calculated from the Morison equation:

$$F_d = \frac{1}{2} \rho C_d A u^2 \tag{14}$$

$$F_l = \frac{1}{2} \rho C_l A u^2 \tag{15}$$

where C_d and C_l are coefficients that can be calculated using empirical formulas proposed by **Zhan et al. (2006), Løland (1991), Aarsnes et al. (1990),** etc.

When the plane net is oriented normal to the flow, the porous coefficients (D_n and C_n) are chosen from a curve fit between drag force data of the plane net and corresponding current velocities using the least squares method. The other two coefficients (D_t and C_t) can be ignored because the lift force is equal to 0 when a=90°.

When the plane net is oriented with different attack angles (see Fig. 6), the porous coefficients should be transformed into formula (16) **(Bear, 2006)**. Then, the four porous coefficients can be obtained by minimizing the error between the theoretical values and existing data for the drag and lift forces using the least squares method, which is a common analytical method in error minimization.

$$\begin{aligned} D_n^{'} &= \frac{D_n + D_t}{2} + \frac{D_n - D_t}{2} \cos(2\alpha^{'}); D_t^{'} = \frac{D_n - D_t}{2} \sin(2\alpha^{'}); \\ C_n^{'} &= \frac{C_n + C_t}{2} + \frac{C_n - C_t}{2} \cos(2\alpha^{'}); C_t^{'} = \frac{C_n - C_t}{2} \sin(2\alpha^{'}). \end{aligned} \tag{16}$$

where $\alpha^{'} = 90^0 - \alpha$, and a is the attack angle.

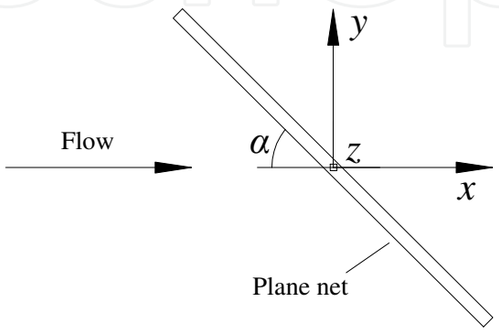

Fig. 6. Definition of attack angle (a).

2.3.2 Mesh grids and boundary conditions

An example of computational grids of a plane net at an attack angle a=90° is shown in Fig. 7. The mesh consists of unstructured tetrahedral elements that are refined in the vicinity of the porous media. The coordinate system for the numerical model is a right-handed, 3D Cartesian coordinate system, where x is positive toward the flow direction. The left boundary of the flume tank is described by the velocity-inlet boundary condition, while the right boundary is described by the outflow boundary condition. The solid surfaces of the flume tank and the free surface are modeled using the wall boundary condition (with zero shear force).

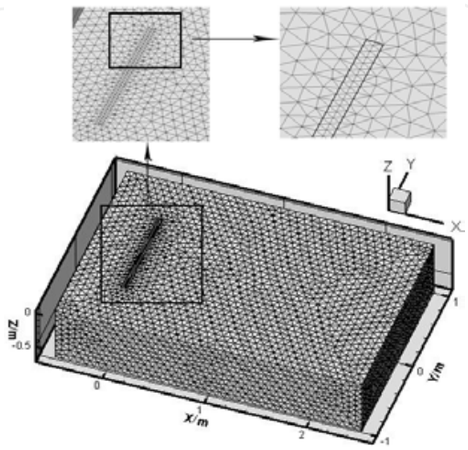

Fig. 7. Example of the computational grids.

3. Hydrodynamic simulation of net cage in irregular waves

The real sea is mainly composed of irregular waves. In this section, the hydrodynamic behavior of net cage in irregular waves is analyzed by numerical simulation and physical model test.

3.1 Irregular wave model

The linear wave theory (refer to **Zhao et al. 2007**) and random phase method are employed in the computation of irregular wave field. Based on linear wave theory, the velocity potential of the wave is given by

$$\phi = -A\frac{g}{2\pi f}\frac{\cosh k(d+z)}{\cosh kd}\sin(kx - 2\pi ft) \tag{17}$$

Surface elevation,

$$\eta = A\cos(kx - 2\pi ft) \tag{18}$$

and dispersion relation,

$$(2\pi f)^2 = gk\tanh(kd) \tag{19}$$

where A is the wave amplitude, g is gravitational acceleration, f is the wave frequency, k is the wave number (equal to $2\pi/L$), L is the wave length, d is the water depth, z is the vertical distance (positive upward) from mean-water level.

The irregular waves are generated using the random phase method as described by **Charkrabarti (1994)** which, in the time domain, is the superposition of multiple regular waves.

$$\eta(x,t)=\sum_{j=1}^{n}A_j\cos(k_jx-2\pi f_jt+\varepsilon_j) \tag{20}$$

where A_j is given by

$$A_j=\sqrt{2S(f_j)\Delta f} \tag{21}$$

where A_j and K_j are the wave amplitude and number of the individual wave components, respectively. ε_j is the uniform distributive random phase between 0 and 2π. The surface elevation time series will repeat after a given amount of time, and it is correlated with the two aspects: the number of regular waves used in the superposition and the sample length of the surface elevation. In the present study it was decided to discretize to 60 waves in the spectrum and have a length of each time series giving approximately 100 wave cycles. The input wave spectrum $S(f)$ is determined by the modified JONSWAP spectrum given by **Goda (1999)**, as follows,

$$S(f)=\beta_JH_{1/3}^2T_P^{-4}f^{-5}\exp\left[-1.25(T_Pf)^{-4}\right]\cdot\gamma^{\exp\left[-(f/f_P-1)^2/2\sigma^2\right]} \tag{22}$$

where T_P is the spectral dominant period, $T_p=T_{H1/3}/(1\text{-}0.132(\gamma+0.2)^{-0.559})$; $H_{1/3}$ and $T_{H1/3}$ are the significant wave height and period, respectively; f is the wave frequency; f_P is the spectral peak frequency; σ is the peak shape factor, σ=0.07 ($f\le f_P$), σ=0.09 ($f>f_P$), γ is the peak enhancement factor and equal to 3.3. The parameter β_J is determined by the following expression:

$$\beta_J=\frac{0.06238}{0.230+0.0336\gamma-0.185(1.9+\gamma)^{-1}}\cdot\left[1.094-0.01915\ln\gamma\right] \tag{23}$$

3.2 Physical model set up

A series of experiments of the motion response of float collar and the tension response in the mooring line were conducted in a wave-current flume at the State Key Laboratory of Coastal and Offshore Engineering, Dalian University of Technology, China. The wave-current flume is 69m long, 2m wide and 1.8m high, equipped with a random wave-maker and a current-producing system. The test setup is shown in Fig. 8. As shown in the Fig. 8, the physical model was installed in the centre of the flume. The mooring-line forces were measured by two transducers attached to the bottom of the mooring lines. The anchors on the left side are labeled for load identification. An optical measurement system for determining the float collar motions was developed. Two diodes (front and back points), numbered 1 and 2, were fixed on

the float collar for motion analysis. The movement of diodes was recorded by a CCD camera. The camera captures a series of images and transfers each frame to the computer and temporary storage. Later, specially-written software is used to search the position of diodes, which is used to calculate the float collar horizontal and vertical movements as a function of time. The geometric and mechanical properties of gravity cage model are provided in Table 1.

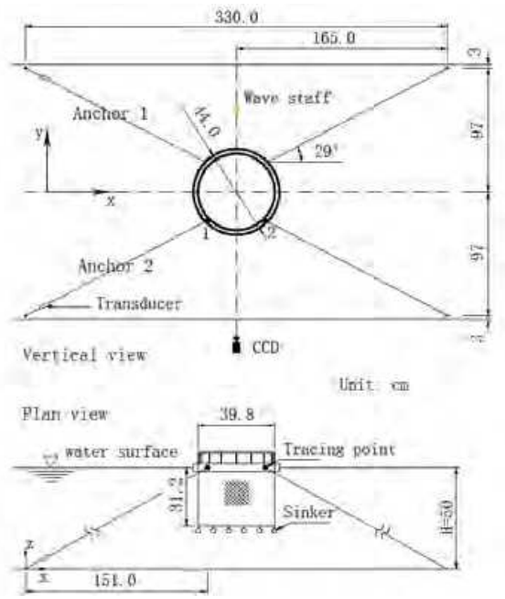

Fig. 8. Arrangement of a gravity cage model in the wave tank

Component	Parameter	value
Outer circle	Circumference(m)	1.382
	Pipe diameter(m)	0.014
	material	HDPE
Inner circle	Circumference(m)	1.250
	Pipe diameter(m)	0.014
	material	HDPE
Net	Mesh size(m)	0.041
	Twine diameter(m)	0.001
	Material	PE
Sinker	Unit mass(g)	1.8
	Number of pieces	10
	Total mass(g)	18.0
Mooring line	Length(m)	1.657
	Diameter(m)	0.00072
	Density(g/cm3)	1.14
	Pretension(N)	1.913

Table 1. Specifications of the physical model

3.3 Comparison in time domain

The numerical and physical gravity cage models were subjected to regular and irregular waves. The motion response (in surge and heave) of the float collar and the tension response in the mooring line are analyzed and compared in the time domain.

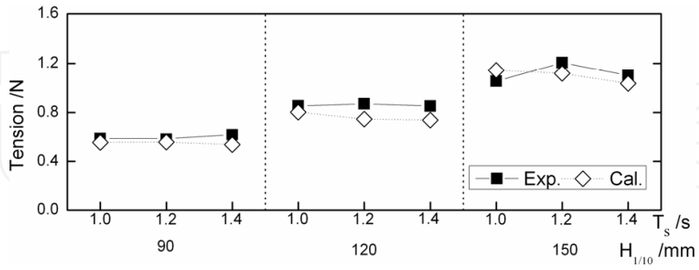

Fig. 9. Comparisons of the average of top one-tenth mooring line forces between numerical and experimental data

To examine the numerical model, quantitative comparisons are carried out between calculated and experimental results. The average of one-tenth highest mooring line tensions and cage motions are selected for comparisons. Fig. 9 shows the comparisons of the average of one-tenth highest mooring line tensions between calculated and experimental results. Fig. 10 and 11 demonstrate comparisons of the top one-tenth cage surge and heave motions between simulated and experimental results, respectively. The mean relative error of the mooring-line forces is 6.9%, and the mean relative errors of the cage surge and heave motions are 9.9% and -4.2%, respectively.

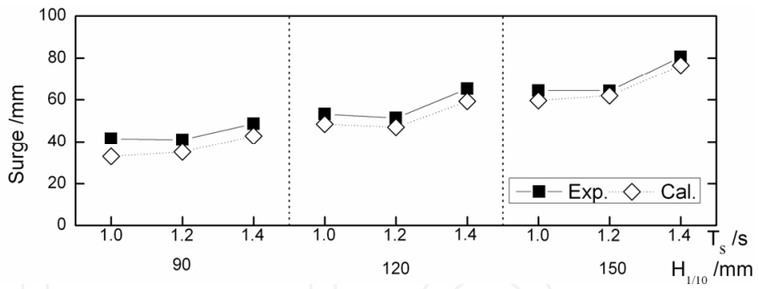

Fig. 10. Comparisons of the average of top one-tenth cage surge motions between numerical and experimental data

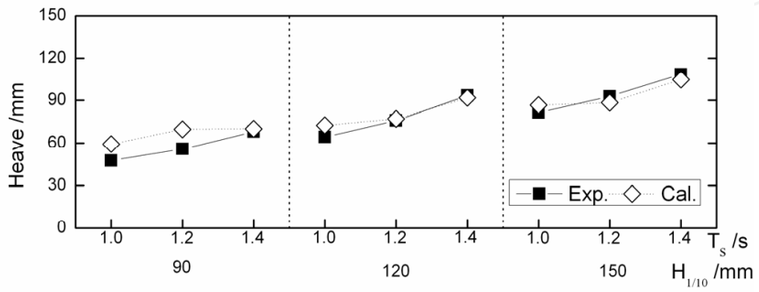

Fig. 11. Comparisons of the average of top one-tenth cage heave motions between numerical and experimental data

3.4 Comparison in frequency domain

For regular wave cases, response amplitude operators (RAOs), determined by dividing the amplitude of the response by the amplitude of the wave, are used to characterize the surge and heave motion response and the mooring-line tension response. For irregular wave cases, the transfer functions of the motion response of the float collar and the tension response in the mooring line were calculated using auto-spectral density method, and compared with the regular wave RAOs. The corresponding transfer functions are calculated as a function of frequency. Combining with statistical wave descriptions, these transfer functions can be used to yield statistics of cage dynamic response in a realistic sea conditions.

The time series of wave elevation and heave motion of float collar from the numerical simulation and physical model tests are shown in Fig. 12. In Fig. 12, the heave motion of float collar is synchronized with the wave elevation. Based on these time series, the corresponding auto-spectral density function can be obtained by using Fast Fourier Transform (FFT) method. The numerical and physical model wave spectra are shown in Fig. 13. The Fig. 13 shows that the wave spectra obtained from the numerical simulation and physical model test are similar to each other.

According to **Bendat and Peirsol (1986)**, the linear transfer functions of cage motion and tension responses can be calculated using the auto-spectral technique.

Fig. 14 shows the heave motion transfer function. In general, the motion response transfer function results for heave were characteristic of a highly damped system. At high frequencies, the cage system has no significant heave motion response to wave forcing. With the decreasing of wave frequency, the heave motion transfer function increases approaching one, indicating wave contouring behavior. This is reasonable, and it agrees with our qualitative analysis according to the common knowledge. In all cases the heave motion transfer function did not exhibit a resonant peak but tend to a value of one as the wave frequency decreases. If a resonant condition exists, it most likely occurs at the waves with frequency lower than 0.6 Hz.

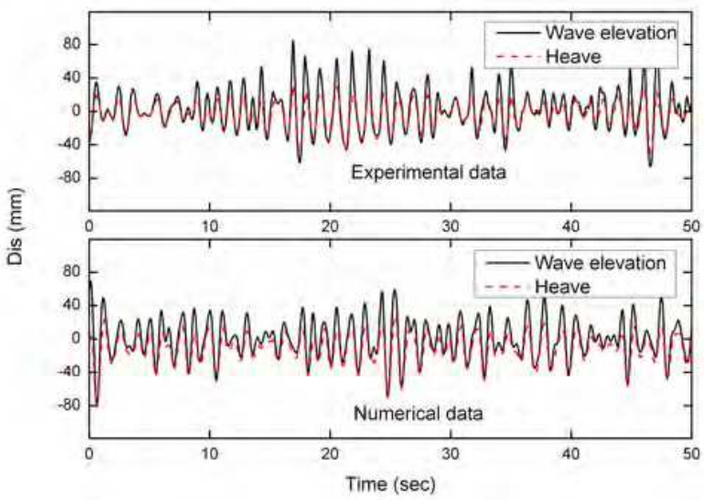

Fig. 12. The time series of wave elevation from the numerical simulation and physical model tests (the average of top one-tenth wave height $H_{1/10}$ is 0.12 m and significant wave period T_s is 1.2 s)

The surge transfer function results are presented in Fig. 15. It shows that the responses of the gravity cage in surge, obtained from the numerical simulation and physical model test, are similar with little response in high frequencies. As with heave motion response, the surge motion tends to increase slightly with decreasing wave frequency.

As shown in Fig. 16, the mooring line tension results, obtained from numerical simulation and physical model test, matched up well throughout the frequencies. The transfer functions of the mooring line tension and the cage motion in heave and surge show the same trend. As the wave frequency increases, the tension response in mooring line decreases. The numerical and physical models both predicted a mooring line tension response less than 0.02 N/mm throughout the wave frequencies.

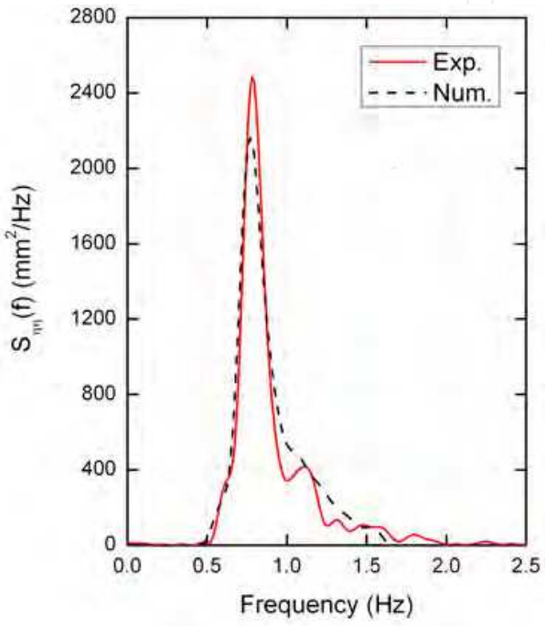

Fig. 13. The output recorded wave spectra of the numerical simulation and physical model test, (H1/10 = 0.12 m, Ts = 1.2 s).

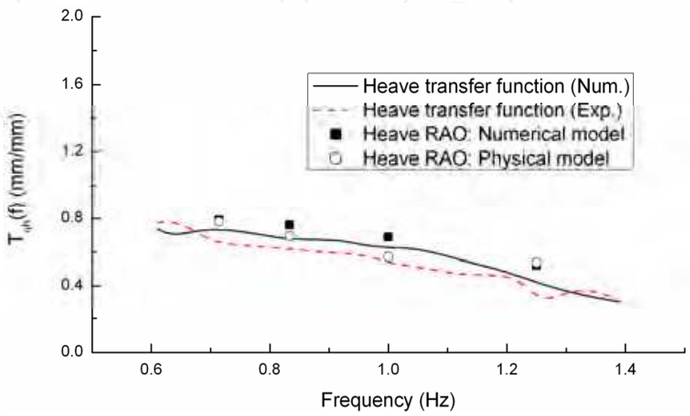

Fig. 14. Heave results from the numerical simulation (random shown by solid line; regular by squares) and physical model tests (random shown by dashed line; regular by circular dots)

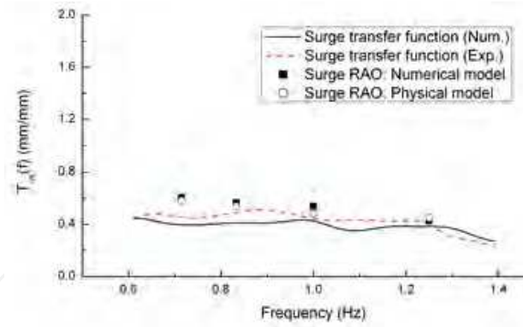

Fig. 15. Surge results from the numerical simulation (random shown by solid line; regular by squares) and physical model tests (random shown by dashed line; regular by circular dots)

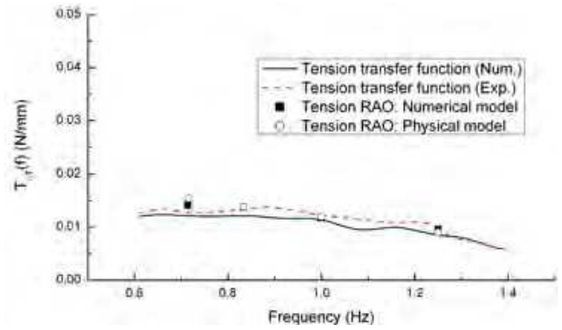

Fig. 16. Mooring line tension results from the numerical simulation (random shown by solid line; regular by squares) and physical model tests (random shown by dashed line; regular by circular dots)

4. Hydrodynamic behavior of multiple net cages

In the open sea, the large fish farm often includes multiple net cages assembly together. In this section, a numerical model of four-cage mooring structure in regular waves is presented. The effect of wave directions on mooring line tensions is analyzed.

4.1 Cage arrangement description

Mooring system is used to hold cage structures against the forces caused by waves and currents. Its design is very important for the operating and performance of cage structures. A change in the mooring system will change the internal loads on the cage systems. In this section, a four-cage system with grid mooring is analyzed. As shown in Fig. 17, four cages are arranged in two columns. Each net cage is connected to the submerged grid mooring by four bridle lines. The submerged grid mooring is attached to the sea floor by anchor lines. The direction of anchor line is perpendicular to grid line, which forms a 16 degree angle with the sea floor. The grid mooring consists of four submerged, pre-tensioned square grid (1 m × 1 m). The horizontal grid is 0.1 m below the still water surface. The pretension on the mooring system is maintained by the submerged floater at each grid corner. The diameter of floating pipe is 6.25 mm, and its density is 7.1 g/m. The diameter of net twine is 0.72 mm, and the mesh size is 11.7 mm.

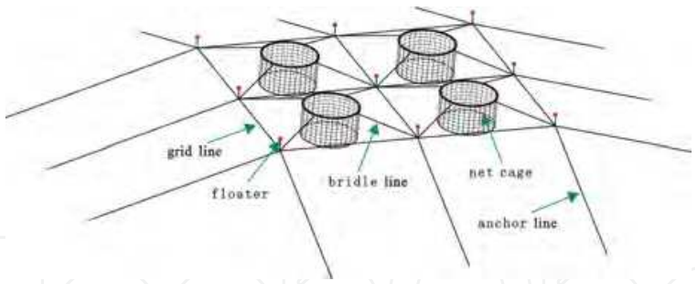

Fig. 17. Offshore grid mooring cage structure

4.2 The effect of wave direction on mooring line tension

Note that the waves propagated along various directions in the open sea, and it will affect the hydrodynamic behavior of grid mooring cage structure. Therefore, three different wave directions are considered in this section. Concerning the symmetrical characteristics of grid mooring cage structures, wave directions of 0°, 30° and 45° are chosen. Since the tension force on anchor lines is largest among the three types of mooring lines, only the maximum tension force on anchor lines is given here for the sake of clarity. Fig. 18 shows the maximum tension force on anchor lines of net cage system under the action of waves from different directions.

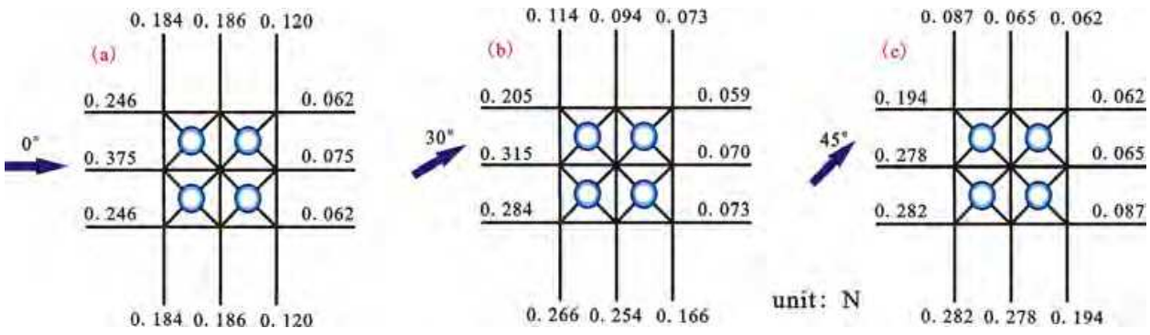

Fig. 18. The maximum tension force on anchor lines of two kinds of mooring cage structures subjected to waves from different directions.

For three different wave directions, the maximum tension forces on anchor lines are 0.375 N, 0.315 N and 0.282 N, respectively. When the wave incident angle is 0°, the left three anchor lines are main components to withstand external force on net cages. If the incident angle becomes 45°, the left three anchor lines and the bottom three anchor lines are main components to withstand the external force. Considering three kinds of wave directions, the uniformity of tension force on anchor lines is different.

When wave incident angle becomes 45°, there are more anchor lines to withstand external force on net cage. Therefore, the maximum tension force on anchor lines is smallest when wave incident angle is 45°.

For different wave incident angles, the transfer load path is different, and hence the uniformity of tension force on anchor lines is different. In the design of mooring cage structure, wave incident angle of 45° may be a good choice.

5. Numerical simulation of flow through and around fishing net cage

In this section, the flow field inside and around a gravity cage is simulated. The diameter of the cage (D) is 16 m, and the height (H) is 10 m. The cage net is knotless nylon net. The twine diameter was 2.8 mm, and the net mesh size was 29 mm. For the numerical model only the fishing net is modeled, and the effect of the float collar and sinker system on the flow field is ignored. The cylindrical cage is divided into 16 plane nets around the circumference and a bottom net (see Fig. 19). These plane nets can be described as the porous media with different attack angles. Therefore, the simulation of the flow field inside and around a gravity cage is straight forward.

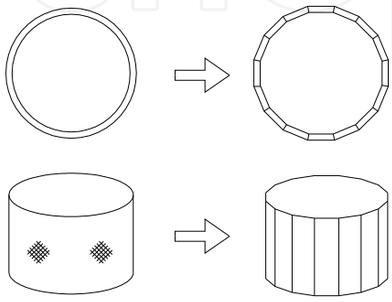

Fig. 19. Sketch of the gravity cage model.

5.1 Numerical model description

In the numerical model, the flume is 240 m long, 80 m wide and the depth of the water is 20 m. The boundary is considered large enough that the influence of the boundary condition on the flow field around the cage is negligible. The thickness of the porous media is 50 mm, and the porous coefficients are D_n=75083 m^{-2}, D_t=38307 m^{-2}, C_n=4.985 m^{-1}, and C_t=1.660 m^{-1}. The numerical simulations are performed with the incoming velocity u_0=0.5 m/s and the inlet turbulence quantities: k=1.34×10^{-4} m^2/s^2 and ε=4.76×10^{-9} m^2/s.

Four cases are modeled with different cage numbers, n=1, 2, 3 and 4, and the spacing distance between two adjacent cages is 24 m. The cages, which are located in a row along the flow direction, are centered on the width of the flume. The front cage is positioned 40 m downstream from the velocity-inlet boundary, while the others are positioned downstream successively with different cage numbers. Fig. 20 shows the sketch of one cage model.

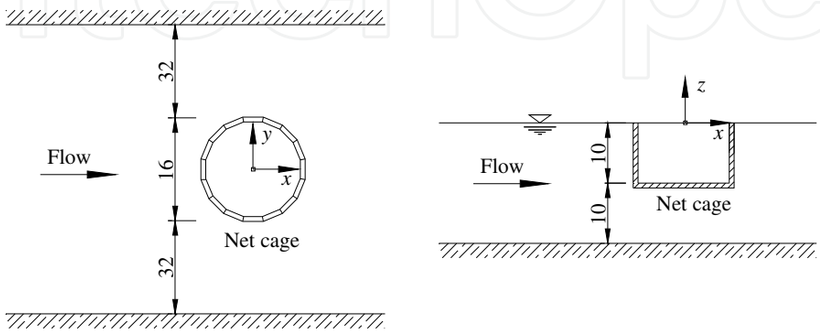

(a) horizontal view (b) vertical view

Fig. 20. Sketch of a gravity cage model (unit: m).

5.2 Simulated results

As shown in the contour plots, the velocity is approximately uniformly distributed inside the cage. There is a small region of velocity reduction upstream of the cage, while there is a rather large velocity reduction region downstream from the cage. Obvious flow velocity reduction exists along the flow direction, and the velocity reduction increases with increasing cage numbers. The width of the wake becomes narrower toward the centerline with increasing distance from the cage. The flow velocities outside the velocity reduction region are approximately 1%–10% greater than the incoming flow u_0, and more cages lead to greater flow velocity around the cages (see Fig. 21). As the cage number increases from 1 to 4, the maximum velocity reduction downstream from the cages increases from 25% to 69%. The cages influence the flow velocity distribution inside and around them. The rear cage has no influence on the flow velocity distribution inside the former cage (see Fig. 22).

Aarsnes *et al***. (1990)** combined theoretical work with the experimental work to derive formulas for flow velocity reduction of the cage nets. The formulas are as follows:

$$u = u_0 \prod_{i=1}^{n_c} r_i \ , \ \ r_i = 1.0 - 0.46 C_d \tag{24}$$

where r_i is the flow velocity reduction factor, n_c is the number of upstream crossings of the cage net, and C_d is the drag coefficient of the net.

The flow velocity reduction factors u/u_0 show a good agreement and the velocity reduction trend of the numerical simulations is consistent with the results of Aarsnes's formula at different cage numbers. Fig. 23 shows the comparison results when n=4.

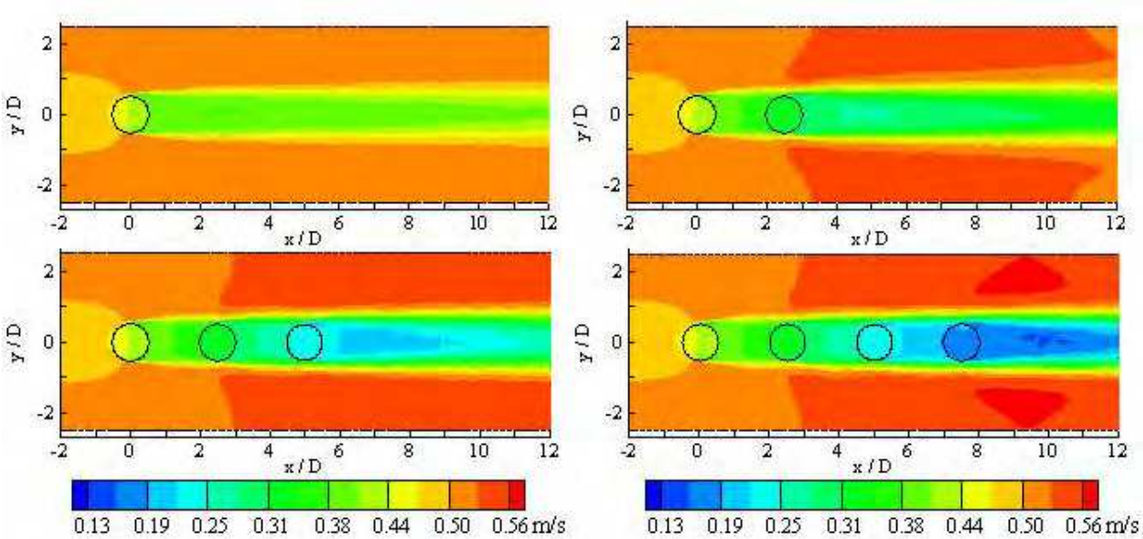

Fig. 21. Velocity distribution on a horizontal cut through the center of the cages at different cage numbers (n=1, 2, 3 and 4).

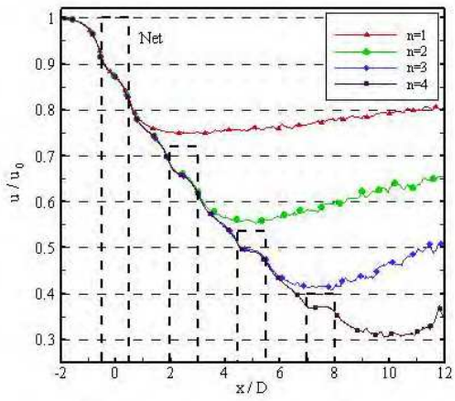

Fig. 22. Magnitude of the flow velocity u along the centerline of the cages in the x direction at different cage numbers (n=1, 2, 3 and 4).

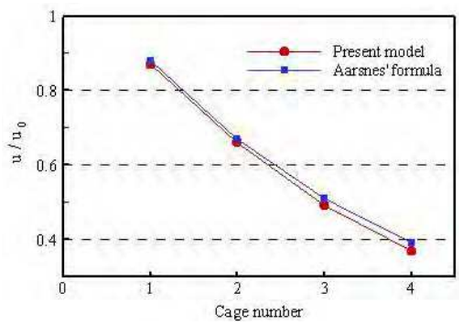

Fig. 23. Comparisons of the flow velocity reduction factor u/u_0 inside the cages between the present numerical model and Aarsnes's formula.

6. Conclusions

Three numerical models for calculating net cage in irregular waves, multi-net cage in waves and flow through fishing net cage are developed in the paper. The simulated results are in good agreement with the experimental values. Some main conclusions can be drawn as follows:

1. The gravity cage system shows a characteristic of a highly damped system with small response to high frequencies. The gravity cage surge and heave motions generally decrease as the wave frequencies increase. The heave motion is synchronized with the wave elevation. At low frequencies, the heave motion transfer function is approaching to one indicating wave contouring behavior. The transfer functions of cage motion response (heave and surge) and mooring line tension response have the same trend.
2. When the wave incident angle is 45°, the maximum tension force on anchor lines is smallest. Therefore, in the design of grid mooring cage structure, wave incident angle of 45° may be a good choice.
3. The velocity is approximately uniformly distributed inside the cage. As the cage number increases from 1 to 4, obvious flow velocity reduction exists along the flow direction, and the velocity reduction downstream from the cages increases from 25% to 69%. However, the rear cage has no influence on the flow velocity distribution inside the former cage.

7. Acknowledgments

This work was financially supported by the National Natural Science Foundation (NSFC) Project No.50809014 and 50921001, the National 863 High Technology Project No.2006AA100301, and the Specialized Research Fund for the Doctoral Program of Higher Education No.200801411094.

8. References

Aarsnes, J.V.; Rudi, H. & Løland, G. (1990). Current forces on cage, net deflection. *In: Engineering for Offshore Fish Farming*, pp. 137–152, ISBN 0727716018, Thomas Telford, London, Oct 17-18, 1990

BEAR J. (1972). *Dynamics of fluids in porous media*. America Elsevier Publishing Company, Inc., ISBN 0486656756, New York, USA

Bendat, J.S. & Peirsol, A.G. (1986). *Random Data: Analysis and Measurement Procedures* (3rd ed.), Wiley, ISBN 0471317330 ,New York

Bhatt, R.B. & Dukkipati, R.V. (2001). *Advanced dynamics*, Alpha Science International, Ltd., ISBN 184265022X, UK

Brebbia, C.A. & Walker, S. (1979). *Dynamic Analysis of Offshore Structures*, Newnes-Butterworths, ISBN 0408003936, London

Charkrabarti, S.K. (1994). *Offshore Structure Modeling*, World Scientific Publishing, ISBN 9810215126 , Singapore

Choo, Y.I. & Casarella, M.J. (1971). Hydrodynamic resistance of towed cables, *Journal of Hydronautics*, Vol. 5, No. 4, (Oct, 1971), pp. 126–131, ISSN 0022-1716

FLUENT (2006). *FLUENT 6.3 User's Guide*. Fluent Inc., Lebanon, NH, USA, Sep, 2006

Fredheim, A. & Faltinsen, O.M. (2003). Hydroelastic analysis of a fishing net in steady inflow conditions, *Proceeding of 3rd International Conference on Hydroelasticity in Marine Technology*, University of Oxford, Oxford, Great Britain, Sep, 2003

Gerhard, K. (1983). *Fiber Ropes for Fishing Gear*, FAO Fishing Manuals. Fishing News Books Ltd., Farnham, UK

Goda, Y. (1999). A comparative review on the functional forms of directional wave spectrum, *Coastal Engineering Journal*, Vol. 41, No. 1, (Mar, 1999), pp. 1–20, ISSN 0578-5634

Løland, G. (1991). *Current force on flow through fish farms*. PhD Dissertation, Division of Marine Hydrodynamics, Norwegian Institute of Technology, ISBN 82-7119-269-8, Trondheim, Norway

Wilson, B.W. (1967). Elastic characteristics of moorings, *ASCE Journal of the Waterways and Harbors*, Division 93(WW4), pp. 27–56, ISSN 0733-950X

Zhan, J.M.; Jia, X.P.; Li, Y.S.; Sun. M.G.; Guo, G.X. & Hu, Y.Z. (2006). Analytical and experimental investigation of drag on nets of fish cages, *Aquacultural Engineering*, Vol.35, No.1, pp. 91–101, ISSN 0144-8609

Zhao,Y.P. ; Li, Y.C. ; Dong, G.H. ; Gui, F.K. & Wu, H. (2008). An experimental and numerical study of hydrodynamic characteristics of submerged flexible plane nets in waves, *Aquacultural Engineering*, Vol. 38, No. 1, pp. 16–25, ISSN 0144-8609

Zhao,Y.P., Li, Y.C., Dong,G.H., Gui,F.K.(2007). A numerical study on dynamic propeties of gravity cage in combined wave-current flow. *Ocean Engineering*. Vol.34,No.(17-18), pp.2350~2363

Zhao,Y.P.,Li,Y.C.,Dong,G.,H.,Gui.,F.,K.,Teng.,B.(2009).The numerical simulation of hydrody namic behaviors of gravity cage in current and waves. *International Journal of Offshore and Polar Engineering*. Vol. 19, No.2, pp. 97-107

Dong,G.H.,Xu,T.J., Zhao,Y.P., Li,Y.C.,Gui,.F.K.(2011) Analysis of hydrodynamic behaviors of gravity net cage in irregular waves. *Ocean Engineering*.Vol.38,No.13,pp. 1545-1554

Dong,G.H.,Hao,S.H.,Zhao,Y.P., Zong,Z.,Gui,.F.K.(2010) Elastic responses of a flotation ring in water waves. *Journal of Fluids and Structures*.Vol.26, No.1, pp.176-192.

Dong,G.H.,Xu,T.J., Zhao,Y.P., Li,Y.C.,Gui,.F.K.(2010) Numerical simulation of hydrodynamic behavior of gravity cage in irregular waves. *Aquacultural Engineering,* Vol. 42, Issue 2, Pages 90-101.

Dong, G.H., Hao, S.H., Zhao, Y.P., Zong, Z.(2010).Numerical analysis of the flotation ring of a gravity-type fish cage. *Journal of Offshore Mechanics and Arctic Engineering*,Vol. 132, Issue 3,pp: 031304-1- 031304-7

Zong,Z.,Hao,S.H., Zhao,Y.P. , Dong,G.H.,Gui,.F.K.(2008). In-plane hydroelastic response of a circular ring in water waves. *Applied Ocean Research*, Vol.30,No.3,pp.208-214.

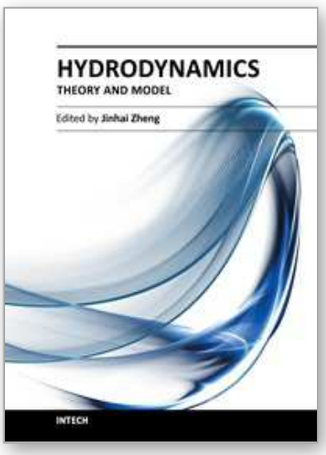

Hydrodynamics - Theory and Model

Edited by Dr. Jin - Hai Zheng

ISBN 978-953-51-0130-7
Hard cover, 306 pages
Publisher InTech
Published online 14, March, 2012
Published in print edition March, 2012

With the amazing advances of scientific research, Hydrodynamics - Theory and Application presents the engineering applications of hydrodynamics from many countries around the world. A wide range of topics are covered in this book, including the theoretical, experimental, and numerical investigations on various subjects related to hydrodynamic problems. The book consists of twelve chapters, each of which is edited separately and deals with a specific topic. The book is intended to be a useful reference to the readers who are working in this field.

How to reference

In order to correctly reference this scholarly work, feel free to copy and paste the following:

Yunpeng Zhao, Tiaojian Xu, Chunwei Bi, Guohai Dong and Shengcong Liu (2012). The Numerical Simulation of Hydrodynamics of Fishing Net Cage, Hydrodynamics - Theory and Model, Dr. Jin - Hai Zheng (Ed.), ISBN: 978-953-51-0130-7, InTech, Available from: http://www.intechopen.com/books/hydrodynamics-theory-and-model/the-numerical-simulation-of-hydrodynamics-of-fishing-net-cage

INTECH
open science | open minds

InTech Europe
University Campus STeP Ri
Slavka Krautzeka 83/A
51000 Rijeka, Croatia
Phone: +385 (51) 770 447
Fax: +385 (51) 686 166
www.intechopen.com

InTech China
Unit 405, Office Block, Hotel Equatorial Shanghai
No.65, Yan An Road (West), Shanghai, 200040, China
中国上海市延安西路65号上海国际贵都大饭店办公楼405单元
Phone: +86-21-62489820
Fax: +86-21-62489821

IntechOpen